https://doi.org/10.3311/PPci.45830
Creative Commons Attribution

Periodica Polytechnica Civil Engineering

Measurement-supported CFD Modeling of Vapor Transport in an Indoor Swimming Pool

Péter Nagy-György[1*]

[1] Department of Hydrodynamic Systems, Faculty of Mechanical Engineering, Budapest University of Technology and Economics, Műegyetem rkp. 3., H-1111 Budapest, Hungary
[*] Corresponding author, e-mail: nagy-gyorgy.peter@gpk.bme.hu

Received: 01 August 2026, Accepted: 13 November 2026, Published online: 17 November 2026

Abstract

Indoor swimming pools require reliable control of air temperature, relative humidity, and outdoor-air supply to ensure thermal comfort, limit condensation and corrosion, and reduce the energy demand of ventilation and dehumidification systems. However, airflow and vapor distributions depend strongly on facility geometry, water surfaces, air-supply arrangement, and operating conditions; therefore, a single humidity measurement may not represent conditions throughout the hall. This study presents a measurement-supported workflow combining local field observations, operational data from four air-handling units, a Dalton-type pool evaporation model, and full-room computational fluid dynamics to analyze vapor transport and identify candidate humidity-sensor locations in a large indoor pool hall with approximately 2024 m² of water surface. At the analyzed operating condition, the evaporation rate predicted by the Dalton-type model agreed with the value independently determined from the air-handling-unit vapor balance within the measurement uncertainty. A three-dimensional ANSYS CFX model was developed in which humid air was treated as a two-component ideal-gas mixture, buoyancy was included, and turbulence was represented using the SST k–ω model. Two air-supply distributions were compared at an unchanged total supply flow rate. Relative to the 1:1 split, the 3:1 spectator-to-pool-side split weakened pool-side mixing, modified ceiling-level low-velocity regions, and increased humidity accumulation near the teaching-pool corner. The integrated workflow linked the building-system vapor balance to pool-specific CFD source terms and identified internal columns at approximately 2.5 m height as promising sensor locations because they avoid direct supply jets while remaining exposed to representative pool-space conditions.

Keywords

computational fluid dynamics, building ventilation, humidity, swimming pool, evaporation

1 Introduction

Indoor swimming pools require continuous control of air temperature, relative humidity and fresh air supply. The ventilation and dehumidification system influences thermal comfort, draft risk, condensation, corrosion, and the durability of building elements. The same system also determines a major part of the operating cost because the air-handling units must heat, dehumidify and circulate large fresh air volumes. In the present period of high energy prices, humidity control based on representative measurements is therefore not only an architectural and building-services problem but also an operational one. Since the swimming-pool designs and operating schedules usually differ, general rules for design and operation are difficult to define.

Existing design approaches address the problem at different levels of resolution. Handbooks and standards provide practical procedures for estimating the global moisture load. ASHRAE [1] and VDI 2089 [2] express evaporation mainly through water-surface area, the vapor-pressure difference between the surface and room air, and an activity-dependent coefficient. Shah [3] reviewed a broad set of correlations and emphasized the distinction between occupied and unoccupied conditions. Controlled scale-model experiments provide complementary evidence: Asdrubali [4] measured evaporation from a reduced-scale pool in a climatic chamber while varying water temperature, air temperature, relative humidity, and air velocity, and developed an engineering prediction model. These approaches are useful for equipment sizing and global load estimation, but they do not identify local high-humidity regions, supply short-circuiting, recirculation, or potentially unrepresentative sensor positions.

Cite this article as: Nagy-György, P. "Measurement-supported CFD Modeling of Vapor Transport in an Indoor Swimming Pool", Periodica Polytechnica Civil Engineering, 2026. https://doi.org/10.3311/PPci.45830

Computational fluid dynamics (CFD) has consequently become an important complement to empirical load calculations. Foncubierta Blázquez et al. [5] proposed a practical single-phase methodology that avoids resolving the liquid pool while retaining vapor generation at the water surface. It was experimentally validated [6] and subsequently enhanced [7]. Full-scale studies have shown that coupled airflow, heat, and species transport can reproduce relevant indoor-pool trends when boundary conditions are supported by measurements [8, 9], while CFD comparisons of air-distribution concepts demonstrate that inlet arrangement can alter ventilation performance even at unchanged total flow [10]. Foncubierta Blázquez et al. [11] further showed that turbulent species diffusivity, particularly the turbulent Schmidt number, materially affects evaporation predictions. More recent studies extend these findings: Proulx et al. [12] numerically examined the effects of modified ventilation strategies on evaporation and thermal comfort, and Royer et al. [13] assessed air-water-interface boundary conditions across different convection regimes.

Despite this progress, three practical gaps remain. First, evaporation coefficients selected from design handbooks are rarely checked against concurrent operational data from the air-handling system. Second, point measurements are often used for validation without distinguishing global mass-balance consistency from local spatial agreement. Third, CFD results are seldom translated into explicit guidance for control-sensor placement.

The present work addresses these research gaps through a large operational case study, building on previously reported CFD modeling of the same facility [14]. Its contribution is an integrated workflow that connects four scales: (i) local field observations, (ii) a building-system vapor balance derived from four air-handling units, (iii) pool-specific vapor source terms, and (iv) a full-room CFD model used to compare operating modes and screen humidity-sensor locations. The field measurements are used to characterize the operating state and support range-level plausibility assessment rather than pointwise validation. The resulting workflow is intended to support ventilation balancing and the selection of representative sensor locations in large indoor pool halls.

The rest of the paper is organized as follows. First, the investigated swimming-pool facility, the air-handling system and the on-site measurement campaign are described, together with the limitations and uncertainty of the measured data in Sections 2.1 and 2.2. Next, the evaporation rate is estimated using both an air-handling-unit vapor balance and a Dalton-type pool-surface model, and the agreement between the two approaches is assessed in Section 2.3. The development of the three-dimensional CFD model is then presented in Section 2.4, including the geometry, computational mesh, physical assumptions, boundary conditions, and investigated air-supply distributions. Subsequently, the numerical results are evaluated in terms of airflow patterns, low-velocity regions, relative-humidity distributions, and the sensitivity of the indoor environment to the supply-air distribution in Section 3. Based on these findings, possible locations for humidity sensors are discussed in Section 4 from both flow-representativeness and practical installation perspectives. Finally, the main conclusions, limitations of the study, and recommendations for further measurements and model development are summarized in Section 5.

2 Materials and methods

2.1 Description of the facility

The investigated facility is the Lővér indoor swimming-pool hall in Sopron, Hungary. The common air volume contains one 50 m competition pool, one 25 m pool, two teaching pools, and two circular whirlpools. The total water surface is 2024 m^2. The spectator stands occupy one long side of the hall, while a glazed facade and pool-side supply system extend along the opposite side. Ceiling beams and distributed extract grilles create a geometrically complex upper zone. Fig. 1 shows the simplified facility layout.

Four air-handling units (AHUs), denoted L1A–L1D, are installed in pairs. Under nominal operating conditions, each unit extracts and supplies approximately 20,000 m^3/h of air, resulting in total extract and supply airflow rates of approximately 80,000 m^3/h. The operational dataset covered 2 December 2025 15:02 to 3 December 2025 15:00 at approximately one-minute resolution and contained supply and extract temperature, relative humidity, and volume flow rate for each unit. The stated supervisory-system measurement accuracies were ±0.1 percentage point for relative humidity, ±0.1 °C for temperature, and ±0.1% of reading for volume flow rate. These specifications were used as input errors in the uncertainty analysis of the calculated vapor mass flows. The resulting errors were evaluated using the conventional first-order root-sum-square propagation method, assuming independent temperature, relative-humidity, and volume-flow measurement errors.

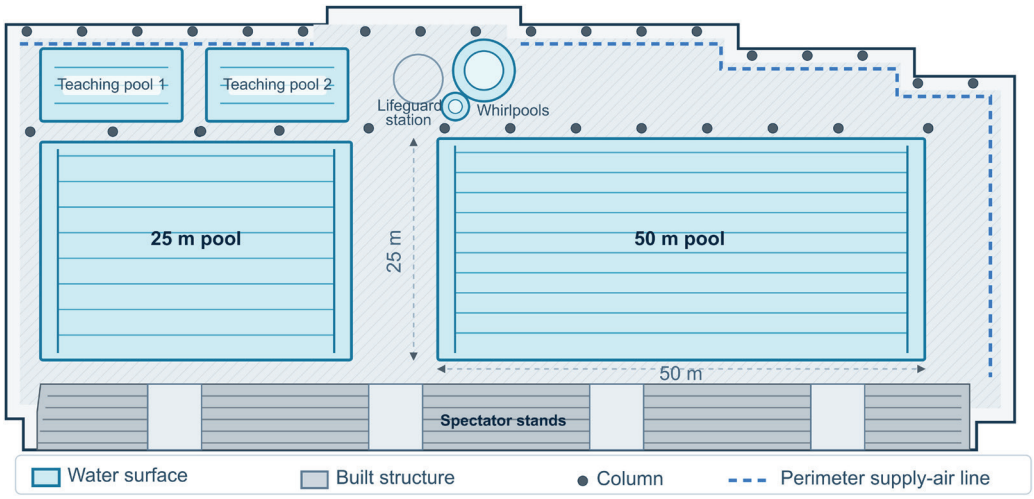


Fig. 1 Simplified facility layout

2.2 Instrumentation and measurement protocol

The field campaign was performed on 3 December 2025. Air speed and temperature were measured with a Testo 440 hot-wire instrument. Its specified velocity range is 0–30 m/s, with an accuracy of ±(0.03 m/s + 0.02 m/s of reading) from 0 to 20 m/s and a resolution of 0.01 m/s. Relative humidity and temperature were measured with a Testo 625 instrument over 0–100% RH, with a stated accuracy of ±2.5 percentage points in the 5–95% RH range and a resolution of 0.1 percentage point.

The spectator area was sampled in the first, middle, and last diffuser rows of the main sectors, using three or four approximately uniformly spaced diffusers in each row. Velocity and supply-air relative humidity were recorded directly at the diffuser, where the higher speed reduced the relative measurement error. Room relative humidity was also recorded approximately 2 m above the same locations. Temperature was sufficiently uniform at the paired heights that one value was retained at most points. One sector was revisited at the end of the campaign to assess short-term variation. The measured ranges are summarized in Table 1.

2.3 Estimation of the water-vapor load

The water-vapor load of the pool hall was determined using two independent approaches. First, the evaporation rate was estimated from the geometry and operating temperature of each pool using a Dalton-type mass-transfer model. Second, the net moisture load was calculated from the measured thermodynamic states and volume flow rates of the supply and extract air streams of the four air-handling units (AHUs). The two estimates were subsequently compared to assess the consistency of the global moisture balance.

Table 1 Quantitative summary of the field measurements

Quantity	n	Range	Mean value	Interpretation
Spectator area				
Supply velocity	62	0.03–3.10 m/s	0.576±0.05 m/s	30 points in 0.2–0.5 m/s; 6 points >1 m/s
Supply RH	62	35.2–53.6 %	44.3±2.5 %	strong sector-to-sector non-uniformity
Far-field RH	62	50.6–62.0 %	55.4±2.5 %	lower spread after room mixing
Pool hall				
jet velocity	64	0.80–4.01 m/s	2.34±0.05 m/s	localized jet maxima
Far-field RH	36	48.1–75.0%	57.9±2.5 %	bulk mainly 54–60 % 70–75 % above water

2.3.1 Evaporation rate calculated from pool data

A Dalton-type expression was applied separately to each of the six water surfaces. The mass flux depends on the difference between saturation vapor pressure at the water temperature and the vapor partial pressure of the bulk air:

$$m_i'' = k_{m,i}\left(p_{sat}\left(T_{w,i}\right) - RH_\infty p_{sat}\left(T_{air}\right)\right), \quad (1)$$

where m_i'' is the evaporated-water mass flux from pool i, k_m is the empirical mass-transfer coefficient, $T_{w,i}$ is the water-surface temperature, T_{air} is the bulk-air temperature, RH_∞ is the bulk relative humidity, and p_{sat} is the saturation vapor pressure.

Saturation pressure was evaluated using the Antoine equation, originally introduced by Antoine [15], in the following natural-logarithm form:

$$p_{sat}\left(T\right) = 1000\left[Pa\right] exp\left[A - B/\left(T + C\right)\right]. \quad (2)$$

In Eq. (2), T is in °C and p_{sat} is in Pa. The coefficients A = 16.3872, B = 3885.70 °C, and C = 230.17 °C were taken from Demirel [16]. In this natural-logarithm form, the exponential term gives pressure in kPa and the factor 1000 converts it to Pa.

The coefficient k_m combines surface activity, water motion, and unresolved near-surface transfer. VDI 2089 [2] and other engineering sources use different categories and units, but their converted values indicate that usage can change the coefficient by several times. For the operating condition considered in the comparison, a uniform k_m = 2.0 × 10⁻⁸ kg/(m² s Pa), room temperature 27.3 °C, and room RH 55% were used. Pool temperatures were 26.5–27 °C for the swimming pools, 32 °C for the teaching pools, and 33 °C for the whirlpools. The value of k_m was selected based on VDI 2089 [2], with the coefficient expressed in the units used in Eq. (1).

The evaporation rate associated with each pool was then obtained by multiplying the mass flux by the corresponding water-surface area, and the total pool-hall evaporation rate was calculated as

$$\dot{m}_{evap} = \sum_{i=1}^{6} m_i'' A_i \,. \tag{3}$$

The resulting total was 234.12 kg/h (see Table 2). The larger pools dominate the absolute load because of their surface area: the 50 m pool contributes 56.7% and the 25 m pool 30.4%. The teaching pools and whirlpools have approximately twice the mass flux per unit area of the swimming pools, but their combined area is small. This distinction is relevant for control: the warm pools can create intense local plumes even though they contribute less to the global moisture balance.

2.3.2 Air-handling-unit vapor balance

An independent evaporation estimate was obtained from the measured supply and extract air states. For each stream, water-vapor partial pressure was calculated from relative humidity and saturation pressure. The water-vapor mass fraction was then evaluated as

$$Y_{water} = \frac{RH p_{sat}\left(T_{Air}\right) M_w}{RH p_{sat}\left(T_{Air}\right) M_w + \left(p_{tot} - RH p_{sat}\left(T_{Air}\right)\right) M_{d,air}} \tag{4}$$

where M_w = 0.018015 kg/mol and $M_{d,air}$ = 0.02897 kg/mol are the molar masses of water vapor and dry air. Here, the temperature T_{air} and total pressure p_{tot} are measured at the extract or supply port of the air-handling unit. The humid-air mixture density was calculated from the ideal-gas equation using the mixture molar mass. The vapor flow of each stream is calculated as the product of the mixture mass flow rate $\dot{m}_{mix} = Q\rho_{mix}$ and the water-vapor mass fraction Y_{water} for each unit (i = 1, 2, 3, 4) and each port (@ extract, @supply)

$$\dot{m}_{removed} = \sum_{i=1}^{4} \dot{m}_{w,i,@extract} - \sum_{i=1}^{4} \dot{m}_{w,i,@supply} \,, \tag{5}$$

where $\dot{m}_{w,i}$ is the water-vapor mass flow rate at the ports of the ith AHU

$$\dot{m}_{w,i} = Q_i \rho_{mix,i} Y_{water,i} \,. \tag{6}$$

The calculation was performed using the time-averaged state of each unit, and the results are summarized in Table 3. The extract-side vapor flows exceeded the corresponding supply-side flows for all units, but the differences were not uniform. Unit L1C accounted for almost half of the total, suggesting that identical units and control logic do not imply identical moisture transport when the connected room regions and inlet states differ.

Errors in the calculated vapor mass flows were determined from the stated temperature, relative-humidity, and volume-flow measurement accuracies using conventional first-order root-sum-square error propagation. The input

Table 2 Pool characteristics and Dalton-model evaporation contributions

Pool type	Size, m	Area, m²	T, °C	Mass flux, kg/(m² h)	Rate, kg/h	Share, %
50 m pool	50 × 25	1250	26.5	0.1062	132.81	56.7
25 m pool	25 × 25	625	27.0	0.1138	71.09	30.4
Teaching 1	10.5 × 6	63.0	32.0	0.2000	12.60	5.38
Teaching 2	10.5 × 6	63.0	32.0	0.2000	12.60	5.38
Large whirlpool	D 5	19.6	33.0	0.2200	4.32	1.85
Small whirlpool	D 2	3.1	33.0	0.2200	0.69	0.30
Total	—	2024	—	—	234.12	100.0

Table 3 Time-averaged air-handling-unit states and vapor-balance contributions calculated from the mean input states

	Extract			Supply			
Unit	RH, %	T, °C	Q, m³/h	RH, %	T, °C	Q, m³/h	Removed vapor, kg/h
L1A	56.7	26.4	20 439	34.2	33.4	19 985	40.05±2.30
L1B	56.2	26.5	20 439	47.6	27.8	19 984	31.43±2.30
L1C	58.6	26.5	20 441	40.7	25.0	19 987	114.22±2.13
L1D	55.1	26.5	20 443	36.1	31.1	19 986	49.67±2.21
Total	—	—	81 762	—	—	79 942	**235.37±4.48**

errors were assumed to be independent. Based on the time-averaged AHU states, the propagated error of the total vapor balance was ±4.48 kg/h, corresponding to ±1.9% of the calculated total. The slight difference between the measured supply and extract volumetric flow rates results from the temperature-dependent difference in air density and does not represent an air-mass imbalance.

The balance was also evaluated at each sampling time. The resulting instantaneous evaporation rate was used to infer an equivalent time-dependent k_m by rearranging Eq. (1). Uncertainty in the inferred k_m therefore combines the AHU measurement uncertainty with the uncertainties of pool-water temperature, bulk-air temperature, relative humidity, water-surface area, and any unmeasured balancing airflow.

2.4 Numerical model

2.4.1 Geometry and mesh

The three-dimensional flow domain was reconstructed from architectural plans, sections, and ventilation drawings. Major bounding surfaces include the concrete and glazed walls, ceiling, pool water surfaces, and floor. Ceiling beams and extract grilles were represented explicitly; the grille resistance was modeled with a porous subdomain. The stepped spectator rows and circular diffusers were retained, while the pool-side linear supply was simplified as rectangular strips. Glass railings, columns, and sector entrances were included because they influence recirculation and local separation. The boundary box has a length of 36.315 m, a maximum domain width of 95.5 m, and a minimum height of 11.5 m. Figs. 2–5 show the geometry from above (Fig. 2), from below (Fig. 3), from an internal viewpoint (Fig. 4), and the refined mesh near the spectator area (Fig. 5).

The mesh contained 31.4 million cells, including 28 750k tetrahedra, 2 568k prisms, and 74k pyramids. Three to five prismatic inflation layers were generated near the principal boundaries, with local refinement around supply openings, railings, columns, spectator steps, and geometric intersections. The minimum orthogonal angle was 11.6°, the maximum expansion factor was 113, and the maximum aspect ratio was 40. The maximum reported y+ value was 4.43.

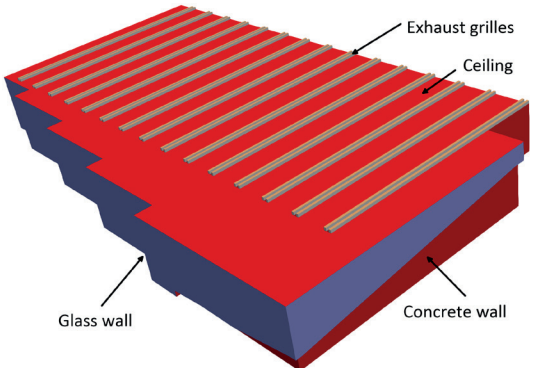


Fig. 2 Geometry viewed from above, showing the walls, ceiling, and exhaust grilles

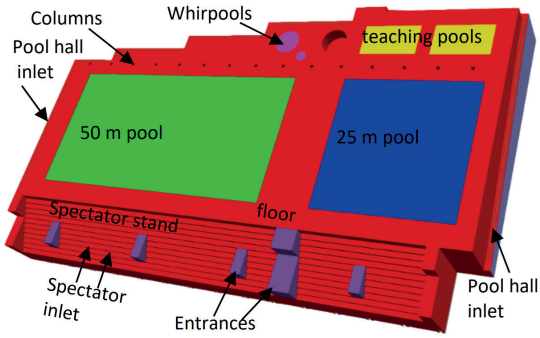


Fig. 3 Geometry viewed from below, showing the pool surfaces, floor, spectator steps, and supply openings

The mean and 95th-percentile values were 1.74 and 3.34 for the glass walls, and 0.52 and 1.13 for the railings, respectively, indicating generally low y+ values on these surfaces.

A mesh sensitivity analysis was performed by approximately halving and doubling the reference mesh cell count while preserving the mesh structure and refinement strategy. Temperature and relative humidity were evaluated at selected locations and the results are presented in Section 3.1.

2.4.2 Physical models and numerical setup

The simulations were performed with ANSYS CFX 2024 R2. The modeled fluid was a variable-composition, two-component ideal-gas mixture of dry air and water vapor. Steady continuity, momentum, thermal-energy, and species-transport equations were solved. Density variation of the humid-air mixture produced buoyancy using a reference density of 1.2 kg/m^3 and gravitational acceleration of

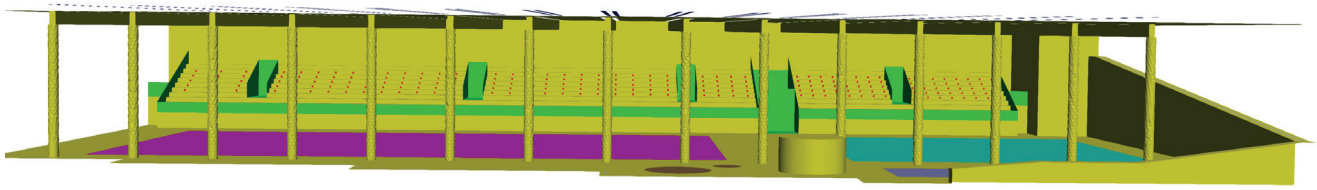


Fig. 4 Internal view of the geometry through the glazed facade

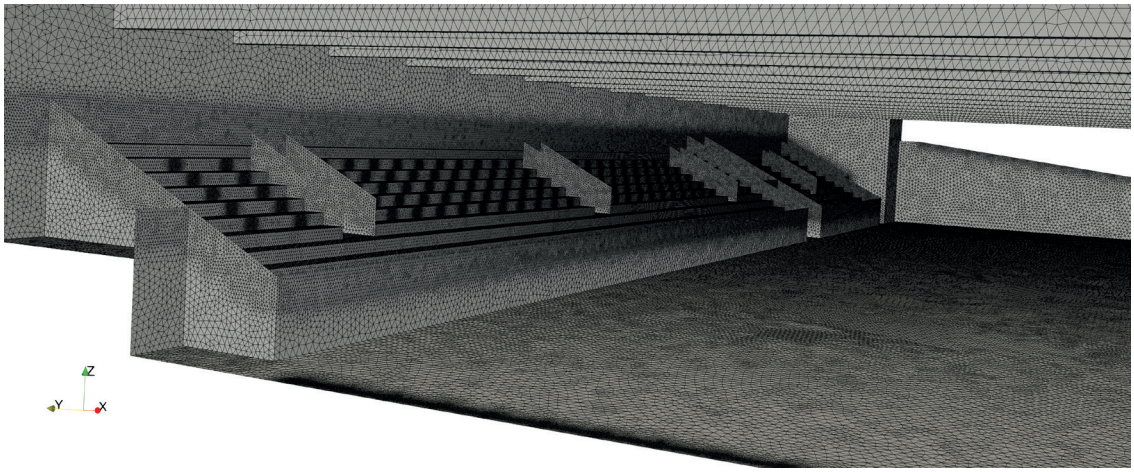


Fig. 5 Internal mesh view showing local refinement near the spectator rows and diffusers

9.81 m/s^2. Turbulence was represented using the SST k–ω model, which combines the near-wall accuracy of the k–ω formulation with the free-stream characteristics of the k–ε model through a blending function. This approach was considered suitable for the investigated pool hall, where airflow is influenced by both wall-bounded regions and large-scale circulation, including flow separation around structural elements and the interaction of ventilation jets with the surrounding air. Thermal radiation was disabled. The liquid-water domains were omitted and vapor was introduced through surface-source terms, consistent with the reduced single-phase approach in [5–7]. The numerical options and CFX defaults reported below follow the software documentation [17, 18].

The modeled spectator-side inlet group comprised 225 circular openings, each with a diameter of 0.30 m, corresponding to a total inlet area of 15.9 m^2. The pool-side supply inlets were represented by 0.050 m-wide strips with a combined modeled length of 158.265 m, resulting in a total inlet area of 7.91 m^2. For the 1:1 airflow split, the corresponding mean inlet velocities were 0.71 m/s at the spectator-side openings and 1.44 m/s at the pool-side strips. For the 3:1 spectator-side-to-pool-side airflow split, the mean velocities were 1.07 and 0.72 m/s, respectively. These velocities were within the measured range. A static temperature of 27.5 °C was specified at both inlet groups.

The extract grilles were assigned a relative static pressure of 0 Pa. Their porous resistance was represented by an isotropic quadratic coefficient of 1.9139 × 10^4 kg/m^4 with no linear term; this value was derived from a 20 Pa pressure drop across a 0.05 m porous thickness at an effective outlet velocity of 0.04572 m/s. The glazed facade was a smooth no-slip wall at 26.5 °C, and the railings were adiabatic no-slip walls. The pool surfaces were free-slip walls with prescribed temperature and vapor source (see Table 4). The remaining grouped surfaces – including the ceiling, concrete surfaces, floor, columns, beams, spectator geometry, and sector-entrance truncation surfaces – were modeled as no-slip walls at 26.5 °C. Thus, the sector entrances were closed truncation boundaries and did not permit mass exchange. Because spatially resolved envelope temperatures were unavailable, the model was not intended to predict condensation. The applied boundary conditions are summarized in Table 4.

The high-resolution advection scheme was used for momentum, energy, and species transport, while the turbulence equations used first-order numerics. A fully coupled pressure–velocity solution procedure was applied with automatic false-transient time scaling and a timescale factor of 1.0. The requested and achieved convergence criterion was an RMS residual of 1 × 10^{-5}.

Table 4 The applied boundary conditions

Location	Flow condition	Thermal condition	Moisture condition
Exhaust grilles	p = 0 Pa	zero-gradient	outflow
Ceiling and walls	no-slip	26.5 °C	impermeable
Railings and internal solids	no-slip	adiabatic	impermeable
50 m pool	free-slip	26.5 °C	0.1062 kg/(m² h)
25 m pool	free-slip	27.0 °C	0.1138 kg/(m² h)
Teaching pools	free-slip	32.0 °C	0.2000 kg/(m² h)
Whirlpools	free-slip	33.0 °C	0.2200 kg/(m² h)
Spectator inlet, Case 1 Case 2	 40 881 m³/h 61 322 m³/h	27.5 °C	42% RH
Pool-side inlet, Case 1 Case 2	 40 881 m³/h 20 441 m³/h	27.5 °C	42% RH

Two cases were evaluated. Case 1 divided the 81 763.5 m^3/h supply equally between the spectator-area openings and the pool-side wall openings. Case 2 used a 3:1 split, increasing the spectator supply to 61 322 m^3/h and reducing the pool-side supply to 20 441 m^3/h. The total volume flow, supply temperature, supply humidity, and water-surface sources were unchanged. The comparison therefore isolates the effect of air-distribution balance rather than total ventilation capacity.

3 Results

3.1 Mesh sensitivity analysis

A mesh sensitivity analysis was conducted to assess the influence of spatial discretization on the numerical results. The reference mesh containing 31.4 million cells was coarsened and refined to obtain meshes with 17.4 million (coarse) and 69.5 million (fine) cells, respectively, while maintaining the same overall mesh structure and refinement strategy. The analysis focused on the predicted temperature and relative humidity, as these quantities are directly relevant to the assessment of indoor environmental conditions and humidity-sensor placement.

The results were evaluated at the exhaust outlet and at four selected internal columns. The outlet was included because the extracted air conditions could be related to the operational measurements of the air-handling units (AHUs). The column locations were selected as potential humidity-sensor positions, as discussed in Section 4.2. Specifically, the 3rd, 6th, 9th, and 12th columns were investigated, counting from right to left in Fig. 4. At each column, a spherical sampling region with a radius of 1 m was defined at a height of 2.5 m, and the volume-averaged temperature and relative humidity were evaluated.

The results are summarized in Tables 5 and 6. The predicted temperatures showed very limited sensitivity to mesh resolution, with a maximum difference of approximately 0.06 °C between the reference and fine meshes. Relative humidity exhibited somewhat greater sensitivity, with absolute differences between the reference and fine meshes ranging from 0.29 to 1.28 percentage points at the investigated column locations and approximately 0.56 percentage points at the outlet. The fine-mesh predictions were consistently lower than the reference values at the four column locations, indicating some remaining mesh sensitivity in the local humidity distribution. In Tables 5 and 6, Ref-C denotes the difference between the reference and coarse mesh results, while Ref-F represents the difference between the reference and fine mesh results.

Nevertheless, the observed differences were relatively small in relation to the overall humidity levels and the variations encountered during swimming-pool operation. Occupant activity, water-surface disturbances, and changing ventilation conditions can introduce additional variability that is not fully represented by the steady-state numerical model. The field measurements were collected under varying operating conditions and were therefore used for a qualitative assessment of the predicted environmental conditions rather than strict pointwise quantitative validation. Consequently, the mesh sensitivity results should be distinguished from experimental validation, as they assess the influence of spatial discretization rather than the overall predictive accuracy of the numerical model.

3.2 Evaporated-water estimation

The global moisture balance was assessed by comparing the pool-surface evaporation estimate described in Section 2.3.1 with the AHU vapor balance described in Section 2.3.2. The AHU balance yielded 235.4±4.5 kg/h, compared with 234.12 kg/h from the pool-surface calculation. The absolute difference was 1.25 kg/h, corresponding to 0.5%. Because this difference was smaller than the propagated AHU measurement error of ±4.48 kg/h, the two estimates were consistent within measurement uncertainty at the investigated operating condition. Although this agreement does not demonstrate that the selected

Table 5 Mesh-sensitivity results for relative humidity at selected locations. Ref-C denotes Reference – Coarse difference, and Ref-F denotes Reference – Fine difference

Location	Coarse RH (%)	Reference RH (%)	Fine RH (%)	Ref-C RH (%)	Ref-F RH (%)
Column 3	60.62	60.70	60.41	0.08	0.29
Column 6	59.90	59.99	59.48	0.09	0.51
Column 9	59.29	59.21	58.35	-0.08	0.86
Column 12	59.05	59.52	58.24	0.47	1.28
Outlet	57.98	57.59	58.15	-0.39	-0.56

Table 6 Mesh-sensitivity results for temperature at selected locations. Ref-C denotes Reference – Coarse difference, and Ref-F denotes Reference – Fine difference

Location	Coarse T (°C)	Reference T (°C)	Fine T (°C)	Ref–C T (°C)	Ref-F T (°C)
Column 3	26.59	26.60	26.60	0.01	0.00
Column 6	26.54	26.55	26.55	0.01	0.00
Column 9	26.49	26.48	26.48	-0.01	0.00
Column 12	26.47	26.47	26.53	0.00	-0.06
Outlet	26.50	26.50	26.49	0.00	0.01

coefficient is universally valid, owing to the simplifying assumptions and neglected effects, it provides a useful global estimate before the surface fluxes are imposed in the CFD model.

The measurement data show that the inferred evaporation load ranged from approximately 100 to 547 kg/h, with a mean value of 235.37 kg/h over the 24-h period. The equivalent k_m varied from 9.2×10^{-9} to 5.3×10^{-8} kg/(m^2 s Pa). Fig. 6 shows a low-load nighttime period, a daytime transition, and a higher and more variable afternoon/evening period.

The AHU measurement uncertainty alone corresponds to approximately 1.9% at the mean operating state. A complete uncertainty interval for k_m was not reported because uncertainties in pool-water temperatures, water-surface areas, the representative room state, and unmeasured balancing airflow were not independently quantified.

3.3 Room-scale flow paths

Fig. 7 compares streamlines colored by relative humidity in the two cases. In both runs, supply air enters from the spectator and pool-side openings, crosses the air volume above the pools, entrains vapor, and reaches the ceiling extract system through large recirculation structures. Dominant vortices form on the pool side of the spectator railing and along the glazed facade. The apparent interaction region moves from the central pool area toward the column line in the 3:1 case.

The available solutions suggest that maintaining total airflow does not guarantee identical room-scale moisture fields. Relative to the 1:1 case, the 3:1 spectator-to-pool-side split shifted the interaction region toward the column line and produced a more persistent humid circulation near the warm-pool corner. Because the total supply flow rate, supply temperature, supply humidity, and pool-surface vapor sources were unchanged, the predicted differences result from the redistribution of inlet momentum between the two supply groups within the assumptions of the steady CFD model.

3.4 Low-velocity regions

Regions with velocity magnitude below 0.01 m/s were extracted as a diagnostic indicator of weak convective exchange and plotted in Fig. 8. Values below 0.0001 m/s were omitted from the visualization to reduce the dominance of near-boundary cells and geometric artifacts. The threshold is not a universal comfort or ventilation-effectiveness criterion, and the extracted regions should be interpreted only as low-velocity zones rather than direct measures of air age or contaminant-removal efficiency.

In both cases, low-velocity regions appear below the ceiling in the central upper zone and near the control-station side of the spectator sector. The 3:1 run shows smaller regions in parts of the ceiling zone but a more pronounced region near the upper sections of the columns along the 50 m pool.

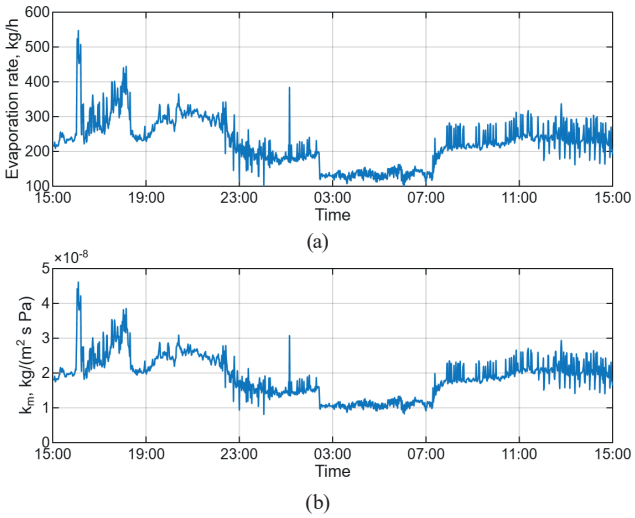


Fig. 6 Operational time series derived from the air-handling-unit balance: (a) total evaporation rate; (b) equivalent mass-transfer coefficient k_m

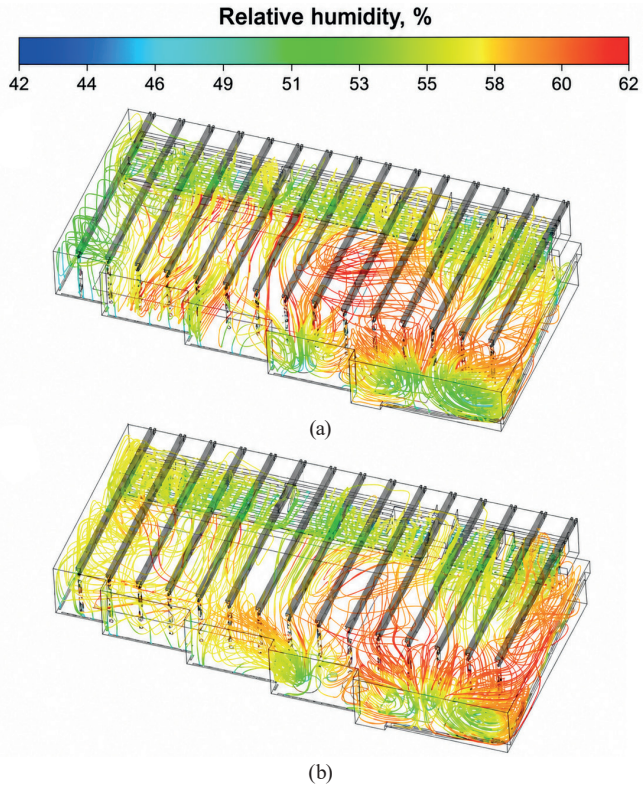


Fig. 7 Streamlines colored by relative humidity for (a) the 1:1 supply split and (b) the 3:1 supply split

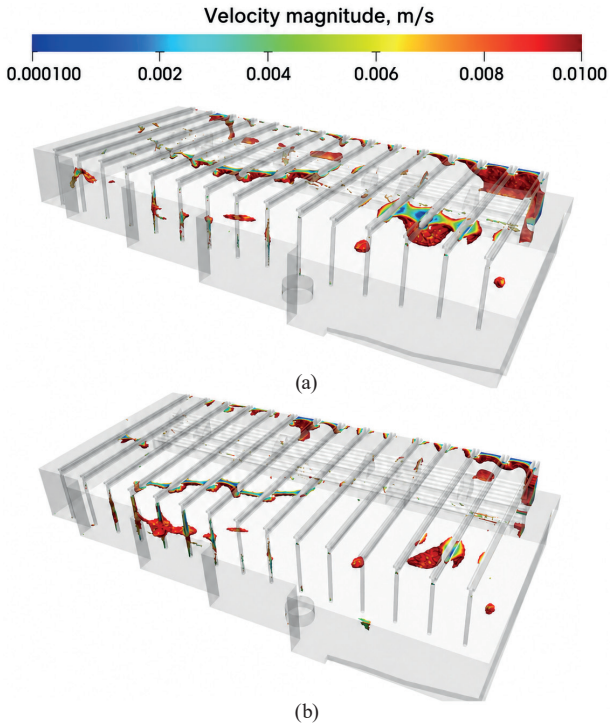


Fig. 8 Regions with velocity magnitude below 0.01 m/s for (a) the 1:1 supply split and (b) the 3:1 supply split

3.5 Relative-humidity and velocity fields

Relative humidity was evaluated on horizontal planes from the water level to the ceiling. Fig. 9 presents the 2.5 m and ceiling-level fields for the two cases. At 2.5 m, both solutions show elevated relative humidity over the pools and lower values near direct supply influence. The computed occupied-zone range is generally consistent with the measured 54–60% range. Near the ceiling, a high-humidity region appears near the teaching-pool corner where no extract grille is located directly above. The region is more pronounced in Case 2, indicating that the reduced pool-side supply weakens local mixing and modifies the transport path from the teaching-pool corner toward the ceiling extract system.

Water-vapor mass fraction was the transported species variable, whereas relative humidity was derived from local vapor partial pressure and temperature. Consequently, a change in relative humidity reflects both moisture redistribution and thermal variation; a cooler region can have higher relative humidity without containing proportionally more water vapor. Relative-humidity contours are presented because they correspond directly to the proposed sensor signal, but physical interpretation of vapor transport must consider the species and temperature fields together. The warm-pool plumes illustrate this coupling: buoyancy transports vapor vertically while temperature modifies the corresponding relative-humidity level.

Velocity contours are shown in Fig. 10. In most of the occupied pool volume, speed remains below 0.5 m/s, consistent with the low and often difficult-to-measure field values away from jets. Higher velocities occur near the spectator-to-pool railing, where recirculating flow is forced upward, and near the supply openings. The 3:1 case increases velocity in the upper part of the spectator-side circulation while reducing penetration from the glazed-wall side. At higher levels, the ceiling beams organize repeated cells that are not apparent from room-average flow rates.

4 Discussion

4.1 Numerical reliability and limitations

The reliability of the numerical approach was assessed at three levels. First, the evaporation rate estimated using the Dalton-type model was compared with the independently determined air-handling-unit (AHU) vapor balance. The calculated evaporation rate of 234.12 kg/h agreed closely

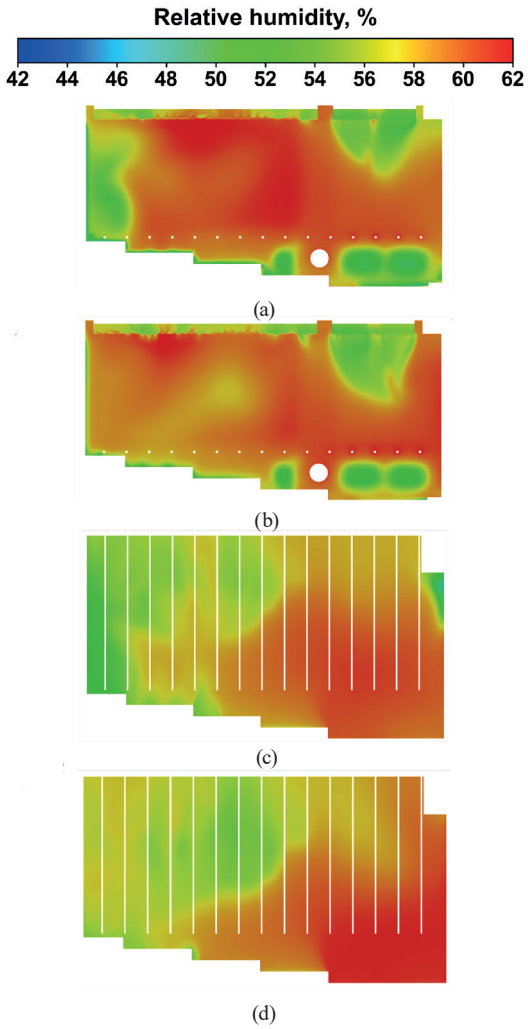


Fig. 9 Relative-humidity contours: (a) 2.5 m, Case 1; (b) 2.5 m, Case 2; (c) ceiling level, Case 1; (d) ceiling level, Case 2

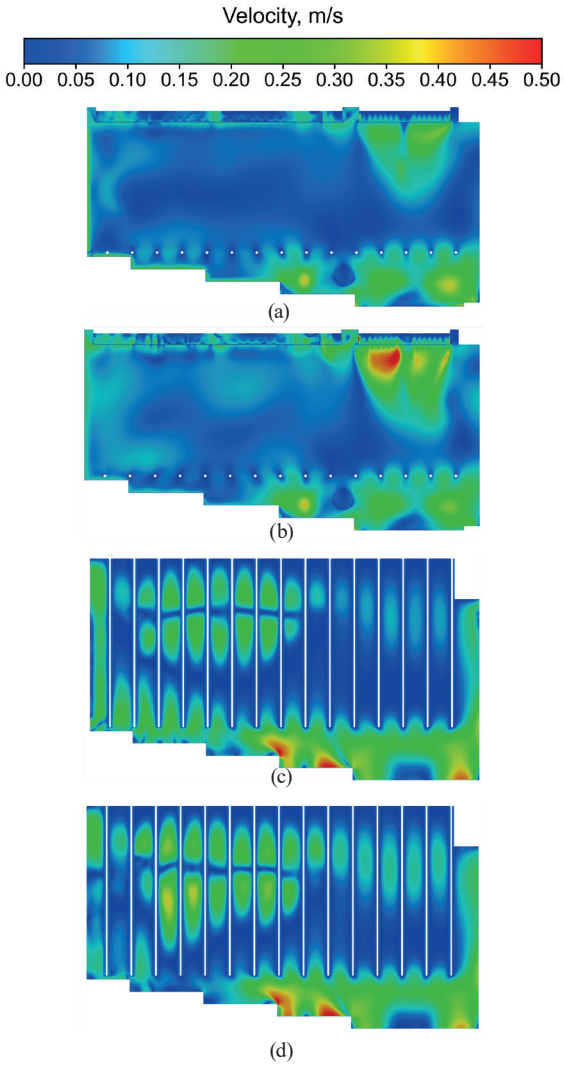


Fig. 10 Velocity-magnitude contours: (a) 2.5 m, Case 1; (b) 2.5 m, Case 2; (c) ceiling level, Case 1; (d) ceiling level, Case 2

with the measured AHU balance of 235.37 ± 4.48 kg/h, with a relative difference of approximately 0.5%. This agreement supports the consistency of the prescribed water-vapor source terms as boundary conditions in the CFD model.

Second, the mesh sensitivity analysis presented in Section 3.1 was used to assess the influence of spatial discretization on the numerical predictions. The temperature differences between the reference and fine meshes were below 0.1 °C at the investigated locations, while the relative-humidity differences reached approximately 1.28 percentage points. These results indicate limited mesh sensitivity for the predicted mean temperature and moderate local sensitivity for relative humidity.

Third, the predicted environmental conditions were assessed against the available field measurements. The calculated occupied-zone relative-humidity levels were generally consistent with the measured range of approximately 54–60%. However, the measurement campaign was not designed for direct pointwise CFD validation. Measurements were collected sequentially under varying operating conditions, while the numerical model employed homogenized inlet boundary conditions and steady-state assumptions.

At the exhaust outlet, the reference-mesh predictions for exhaust-air temperature and relative humidity were 26.50 °C and 57.59%, respectively, which were also close to the measured AHU extract ranges of 26.4–26.5 °C and 55.1–58.6%, respectively. Although the numerical and measured operating conditions were not fully equivalent, this comparison provides additional support for the plausibility of the predicted exhaust-air conditions.

Consequently, the experimental results were used primarily to assess the plausibility of the predicted environmental conditions and general spatial tendencies, rather than to establish pointwise quantitative agreement. Further measurements under controlled and simultaneous operating conditions would be required for a more rigorous quantitative validation of the local airflow and humidity fields.

4.2 Humidity-sensor placement

The sensor-placement assessment considered representativeness, sensitivity to operating changes, accessibility, and vulnerability to local disturbances. Practical installation was assumed at approximately 2.5 m height, mainly on walls or columns. Ceiling suspension was excluded because of maintenance constraints. Seven location families were screened using the field observations and both CFD cases. The glazed facade and spectator walls are poor choices because they are close to dry supply air. The wall on the pool side of the spectator stands is affected by a strong recirculating upflow that can create a noisy signal. Walls beside the 25 m pool are more promising, but a surface-mounted sensor may lie within a wall boundary layer. The teaching-pool walls represent a local buoyant plume rather than the wider hall. The lifeguard enclosure is accessible and humid but includes separation and shielding risks.

Internal columns provide the best compromise. They are sufficiently far from the supply openings to avoid direct-jet bias, yet sufficiently close to the water surfaces to respond to the pool-space moisture load. Columns near the teaching pools can detect the critical humid region, while columns along the middle and lifeguard end of the 50 m pool respond more clearly to the change in supply split. A robust

control system should use more than one sensor: one representative interior sensor for control, supplemented by a sensor near the persistent upper teaching-pool region or by a return-air measurement for supervision. Before control logic is changed, short-term logging at candidate points should verify that the measured signals correlate with occupancy and air-handling-unit operation.

4.3 Value of the integrated workflow

The close agreement of the two global evaporation estimates is the main methodological result. A handbook coefficient by itself can appear precise while carrying large uncertainty; an air-handling-unit balance by itself can be distorted by sensor calibration, outside-air imbalance, or transient storage. Agreement between them provides a defensible basis for imposing pool-specific CFD sources. This division of labor is efficient: the system data constrain the total moisture generation, while CFD resolves spatial redistribution without modeling the liquid water.

The field measurements also show why global agreement must not be confused with local validation. Supply velocities ranged over two orders of magnitude in the spectator area, and supply humidity varied by more than 18 percentage points. The CFD boundary conditions necessarily homogenized these inlets. As a result, the model is suited to comparing the two idealized supply splits and identifying persistent large-scale regions, but it cannot reproduce every measured diffuser or local plume. The distinction should be retained when the model is used for operational decisions.

For building operation, the results indicate that airflow redistribution can be as important as total airflow. Case 2 maintains the same total supply as Case 1 but enlarges the humid teaching-pool corner and changes the location of poorly ventilated volumes. The CFD results are most useful for designing such targeted interventions and defining where additional measurements are needed.

5 Conclusions

A measurement-supported workflow was developed to investigate vapor transport and ventilation performance in a large indoor swimming-pool hall by combining field observations, air-handling-unit data, a pool-surface evaporation model, and full-room airflow and vapor-transport CFD. The Dalton-type calculation predicted an evaporation rate of 234.12 kg/h, while the AHU vapor balance yielded 235.4±4.5 kg/h. The difference was smaller than the propagated AHU measurement error of ±1.9%. The two estimates were therefore consistent within measurement uncertainty at the investigated operating condition. The one-minute AHU balance additionally demonstrated substantial operational variation, with inferred evaporation rates ranging from approximately 100 to 547 kg/h.

The CFD results showed that changing the supply-air split from 1:1 to 3:1 at constant total flow altered the ceiling-level stagnant regions and increased humidity accumulation near the teaching-pool corner because of the weaker pool-side mixing. Based on the predicted airflow and humidity fields, the internal columns at approximately 2.5 m height were identified as the most promising locations for humidity sensors, as these positions avoid direct supply jets while remaining exposed to representative pool-space conditions. The novelty of the study lies in linking a globally verified evaporation estimate with room-scale CFD and using the resulting flow field directly to support sensor-placement and ventilation-balancing decisions. The findings indicate that humidity-sensor positioning and branch-flow balancing should be treated as integral parts of ventilation design and commissioning rather than as secondary instrumentation issues.

Acknowledgement

The author thanks Soproni Vízmű Zrt. for providing access to the facility and for supplying architectural, ventilation-system, and air-handling-unit operational data. The author also acknowledges Dr. Csaba Hős of the Department of Hydrodynamic Systems, for his contribution to the industrial investigation.

References

[1] American Society of Heating, Refrigerating and Air-Conditioning Engineers "2023 ASHRAE Handbook – HVAC Applications", ASHRAE, Atlanta, GA, USA, 2023.

[2] Verein Deutscher Ingenieure "VDI 2089 Blatt 1:2023-09 Building Services in Swimming Baths – Indoor Pools", VDI Verlag, Düsseldorf, Germany, 2023.

[3] Shah, M. M. "Methods for Calculation of Evaporation from Swimming Pools and Other Water Surfaces", ASHRAE Transactions, 120(2), pp. 3–17, 2014.

[4] Asdrubali, F. "A Scale Model to Evaluate Water Evaporation from Indoor Swimming Pools", Energy and Buildings, 41(3), pp. 311–319, 2009.
https://doi.org/10.1016/j.enbuild.2008.10.001

[5] Foncubierta Blázquez, J. L., Maestre, I. R., González Gallero, F. J., Álvarez Gómez, P. "A New Practical CFD-Based Methodology to Calculate the Evaporation Rate in Indoor Swimming Pools", Energy and Buildings, 149, pp. 133–141, 2017. https://doi.org/10.1016/j.enbuild.2017.05.023

[6] Foncubierta Blázquez, J. L., Maestre, I. R., González Gallero, F. J., Álvarez Gómez, P. "Experimental Test for the Estimation of the Evaporation Rate in Indoor Swimming Pools: Validation of a New CFD-Based Simulation Methodology", Building and Environment, 138, pp. 293–299, 2018. https://doi.org/10.1016/j.buildenv.2018.05.008

[7] González Gallero, F. J., Maestre, I. R., Foncubierta Blázquez, J. L., Mena Baladés, J. D. "Enhanced CFD-Based Approach to Calculate the Evaporation Rate in Swimming Pools", Science and Technology for the Built Environment, 27(4), pp. 524–532, 2021. https://doi.org/10.1080/23744731.2020.1868219

[8] Limane, A., Fellouah, H., Galanis, N. "Simulation of Airflow with Heat and Mass Transfer in an Indoor Swimming Pool by OpenFOAM", International Journal of Heat and Mass Transfer, 109, pp. 862–878, 2017. https://doi.org/10.1016/j.ijheatmasstransfer.2017.02.030

[9] Ciuman, P., Lipska, B. "Experimental Validation of the Numerical Model of Air, Heat and Moisture Flow in an Indoor Swimming Pool", Building and Environment, 145, pp. 1–13, 2018. https://doi.org/10.1016/j.buildenv.2018.09.009

[10] Rojas, G., Grove-Smith, J. "Improving Ventilation Efficiency for a Highly Energy Efficient Indoor Swimming Pool Using CFD Simulations", Fluids, 3(4), 92, 2018. https://doi.org/10.3390/fluids3040092

[11] Foncubierta Blázquez, J. L., Maestre, I. R., González Gallero, F. J., Pérez-Lombard, L., Bottarelli, M. "Experimental Adjustment of the Turbulent Schmidt Number to Model the Evaporation Rate of Swimming Pools in CFD Programmes", Case Studies in Thermal Engineering, 41, 102665, 2023. https://doi.org/10.1016/j.csite.2022.102665

[12] Proulx, H., Debia, M., Hallé, S. "Impact of Modified Ventilation Strategies on Water Evaporation Rate and Thermal Comfort in an Indoor Swimming Pool by Numerical Study", Building and Environment, 256, 111462, 2024. https://doi.org/10.1016/j.buildenv.2024.111462

[13] Royer, Q., Guibert, R., Horgue, P., Swadling, A., Debenest, G. "Air-Water Interface Boundary Condition for the Numerical Evaporation Rate Prediction of a Horizontal Water Span under Different Convection Regimes", International Journal of Heat and Mass Transfer, 226, 125438, 2024. https://doi.org/10.1016/j.ijheatmasstransfer.2024.125438

[14] Nagy-György, P. "CFD Modelling of Vapour Transport in an Indoor Swimming Pool", In: Lógó, J., Lengyel, A., Németh, R. K. (eds.) Proceedings of 2nd CEACM Multiscale Modeling of Solids and Fluids Conference 2026, Budapest, Hungary, 2026, pp. 199–202. ISBN 9786151120361 https://doi.org/10.3311/CEACMMSF2026-263

[15] Antoine, C. "Tensions des vapeurs: nouvelle relation entre les tensions et les températures" (Vapor pressures: a new relationship between pressures and temperatures), Comptes Rendus des Séances de l'Académie des Sciences, 107, pp. 681–684, 778–780, 836–837, 1888.

[16] Demirel, Y. "Energy: Production, Conversion, Storage, Conservation, and Coupling", 3rd ed., Springer, Cham, Switzerland, 2021. ISBN: 978-3-030-56164-2. https://doi.org/10.1007/978-3-030-56164-2

[17] Ansys, Inc. "Ansys CFX-Solver Modeling Guide, Release 2024 R2", Canonsburg, PA, USA, 2024. [pdf] Available at: https://ansyshelp.ansys.com/public/Views/Secured/corp/v251/en/pdf/Ansys_CFX-Solver_Modeling_Guide.pdf

[18] Ansys, Inc. "Ansys CFX-Solver Theory Guide, Release 2024 R2", Canonsburg, PA, USA, 2024. [pdf] Available at: https://ansyshelp.ansys.com/public/Views/Secured/corp/v251/en/pdf/Ansys_CFX-Solver_Theory_Guide.pdf